Published in final edited form as:

Nano Lett. 2017 May 10; 17(5): 3282–3289. doi:10.1021/acs.nanolett.7b00995.

Bioresponsive Polyoxometalate Cluster for Redox-Activated Photoacoustic Imaging-Guided Photothermal Cancer Therapy

Dalong Ni[†], **Dawei Jiang**[†,#], **Hector F. Valdovinos**[§], **Emily B. Ehlerding**[§], **Bo Yu**[†,‡], **Todd E. Barnhart**[§], **Peng Huang**[#], and **Weibo Cai**[†,§,//,*]

[†]Department of Radiology, University of Wisconsin-Madison, Wisconsin 53705, United States

[§]Department of Medical Physics, University of Wisconsin-Madison, Wisconsin 53705, United States

[#]Guangdong Key Laboratory for Biomedical Measurements and Ultrasound Imaging, School of Biomedical Engineering, Shenzhen University, Shenzhen, China

[‡]School of Chemical Engineering and Pharmacy, Wuhan Institute of Technology, Wuhan, China

[//]University of Wisconsin Carbone Cancer Center, Madison, Wisconsin 53705, United States

Abstract

Although various types of imaging agents have been developed for photoacoustic (PA) imaging, relatively few imaging agents exhibit high selectivity/sensitivity to the tumor microenvironment for on-demand PA imaging and therapy. Herein, molybdenum-based polyoxometalate (POM) clusters with the highest oxidation state of Mo(VI) (denoted as *Ox*-POM) were designed as novel agents for redox-activated PA imaging-guided photothermal therapy (PTT). Capable of escaping from recognition and capture by the liver and spleen, these renal clearable clusters with ultra-small size (hydrodynamic size: 1.9 nm) can accumulate in the tumor, self-assemble into larger nanoclusters at low pH, and are reduced to NIR absorptive agents in the tumor microenvironment. Studies in 4T1 tumor-bearing mice indicated that these clusters could be employed for bio-responsive PA imaging-guided tumor ablation *in vivo*. Our finding is expected to establish a new physicochemical paradigm for the design of PA imaging agents based on clusters, bridging the conventional concepts of “molecule” and “nano” in the bio-imaging field.

TOC image

[*]Corresponding Author: WCai@uwhealth.org.

Supporting Information

Details of experiments and additional supplementary figures. This information is available free of charge *via* the Internet at http://pubs.acs.org.

Conflict of Interest

The authors declare no competing financial interest.

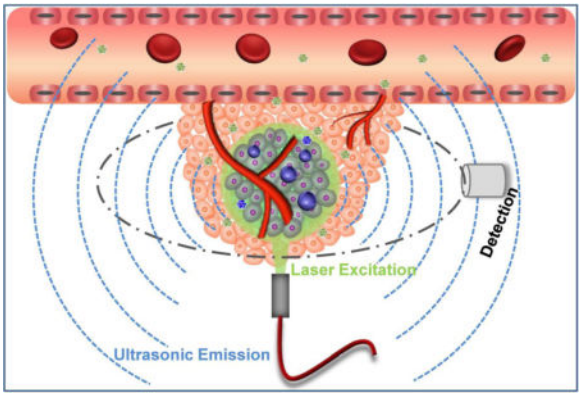

Keywords

Redox-responsive probes; polyoxometalate cluster; photoacoustic imaging; photothermal therapy; theranostic agent

On-demand tumor diagnosis and therapy (i.e., theranostics) trigged by intrinsic physiological microenvironment characteristics (e.g., redox state, pH, enzymes, ions, etc.) have attracted considerable attention in recent years.[1–4] Such therapies can simultaneously reduce the damage of anti-cancer agents to normal tissues and improve their therapeutic efficacy. Among the various physiological parameters, redox status plays a major role in many pathological conditions including chronic inflammation, stroke, and cancer.[5, 6] It has been demonstrated that glutathione (GSH) is the most abundant reducing agent in the tumor, and levels of GSH in cancer tissues are significantly higher than that in normal tissues.[7]

Development of novel imaging methods or probes to detect and monitor redox status *in vivo* is highly desirable. By employing redox-activated molecules or nanoparticle-based probes, various methods for monitoring the redox environment have been reported, including optical imaging with high sensitivity and magnetic resonance imaging (MRI) with high resolution.[8–12] As one of the fastest growing imaging modalities over the past decade, photoacoustic (PA) imaging combines the advantages of high sensitivity of optical imaging and high resolution of ultrasonic imaging.[13, 14] In addition, it can usually be combined with photothermal therapy (PTT) for cancer treatment because both use the same near-infrared (NIR) absorbing materials.[15, 16] However, PA imaging agents with redox-activated diagnostic and therapeutic functions, which could be of high significance for on-demand tumor treatment, have not been developed to date.

Various types of nano-agents have been explored as exogenous agents for PA imaging/PTT, including carbon-based materials,[17–19] gold nanomaterials,[15, 20–23] sulfides,[24–26] and polymeric nanoparticles.[27–30] A common concern about nano-agents for PA imaging is the non-specific uptake of nano-agents by mononuclear phagocyte systems (e.g., liver/spleen) and low accumulation in tumors due to the poor enhanced permeability and retention (EPR) effect. To address this issue, self-assembled PA agents have been designed to remain as small molecules during circulation in the bloodstream and then self-assemble into larger nanostructures in the tumor, triggered by the tumor microenvironment.[31] Various

bioresponsive contrast agents have been developed for PA imaging of reactive oxygen species,[28] enzyme activity,[32,33] pH,[34] and bacterial infection.[30] For example, Dragulescu-Andrasi et al. reported a probe with enzyme-induced self-aggregation, which could provide PA signal to detect enzymatic activity in living subjects.[32] With their self-adaptive electronic structure for enhanced NIR absorption, the Mo-based polyoxometalate (POM) clusters can form larger structures through hydrogen bond formation due to acid-induced protonation.[35, 36] This pH-responsive assembly and photothermal conversion of POM clusters with a size range between “molecule” and “nano” endows them promise as photothermal agents for cancer treatment.[37] The electron relaxation polarization caused by the charge transfer between Mo(VI) and Mo(V) is regarded as the origin of the typical NIR absorption of the POM clusters.[38] The readily reducible characteristics of Mo(VI) into lower oxidation states (*e.g.*, Mo(V)) highlight the potential of POM clusters as an agent for redox-activated bio-imaging.

In this work, we report an intelligent theranostic agent based on POM clusters with the highest oxidation state of Mo(VI) (denoted as *Ox*-POM) for pH-responsive assembly and redox-activated PA imaging-guided PTT (Scheme 1). These *Ox*-POMs show no NIR absorption in their original chemical form, but exhibit strong NIR absorption in the tumor redox microenvironment because Mo(VI) is reduced to Mo(V). The rapidly renal-clearable *Ox*-POM can self-assemble into much larger nanostructures under acidic conditions for enhanced intratumoral accumulation, as demonstrated in our previous work,[37] and herein we further employ the structures as redox-activated agents for PA imaging-guided PTT of cancer. Importantly, these clusters can escape from recognition and capture by the liver and spleen and are mainly excreted through the kidneys, representing an intelligent redox-activated theranostic agent with significant clinical prospects.

The colorless and highly hydrophilic *Ox*-POMs, obtained from an easy, fast, and large-scale synthesis process, were highly stable in various media (Figure S1–S3). Such easy fabrication and large-scale synthesis at a low cost will undoubtedly promote the future investigation of these laboratory-synthesized *Ox*-POMs toward potential clinical studies. The clusters were highly uniform with an average diameter of ~1 nm at pH 7.4 as observed in transmission electron microscopy (TEM) image (Figure 1a). Their energy-dispersive X-ray (EDX) spectrum demonstrated the existence of all the essential chemical elements (Mo, P, and O) of these clusters (Figure S4). Interestingly, these clusters were found to self-assemble into larger but monodisperse spherical assemblies with a diameter of ~25 nm in mildly acidic conditions (pH = 6.5) as TEM showed the collapsed nano-vesicles during the drying process (Figure 1b), suggesting a hollow sphere formation by non-covalent linkage among these cluster blocks.[35, 36] These nano-vesicles were further aggregated into larger structures through additional acidification at pH 5.0 and remained hydrophilic (Figure 1c). This process of pH-responsive self-assembly was also monitored by dynamic light scattering (DLS) measurement (Figure 1d), with their hydrated size increasing from 1.9 nm (pH = 7.4) to 29.3 nm (pH = 6.5) and to ~ 0.43 μm at pH 5.0. Our previous work revealed that the hydrogen bond formation of POM macroanions through acid-induced protonation, with resulting decreased electrostatic repulsions and increased attractive forces, was likely responsible for such pH-driven self-assembly.[37]

Subsequently, the *Ox*-POM clusters were incubated with GSH at different concentrations to evaluate their redox-activated properties. As shown in Figure 1e–f, the pure solution of *Ox*-POM clusters was colorless and exhibited no NIR absorption. After reduction with GSH, the color changed to blue, which deepened monotonically with increasing GSH concentration. The corresponding absorbance showed a peak in the NIR area, which enhanced gradually as the GSH concentration increased (Figure 1f). The same phenomenon was also observed for various concentrations of *Ox*-POM after incubation with a fixed concentration of GSH (Figure 1g, Figure S5). These reduced clusters with blue color exhibited high dispersity in different solvents including deionized water, PBS, FBS and DMEM (Figure 1i). Cysteine (Cys), another reducing agent, was also used as a model to demonstrate the common redox-activated effect of these *Ox*-POM clusters. With the addition of an increasing amount of Cys to the *Ox*-POM solution, the NIR absorption of *Ox*-POM increased gradually as a result of the reduction of Mo(VI) (Figure S6). This enhanced NIR absorption of the *Ox*-POM is founded on the reduction of Mo(VI) to Mo(V) following GSH or Cys incubation. The increased reduction of *Ox*-POM will facilitate the delocalized electron density and occupiable cation site of Mo(V) through the reversible and multiple steps of electron exchange, which will simultaneously strengthen the electron relaxation polarization,[37] leading to enhanced NIR absorption. These *Ox*-POMs couldn't be reduced in the blood, and extremely low hemolysis rate was found after incubation with red blood cells (Figure S7). Also, pH-dependent absorption of *Ox*-POM after GSH incubation was observed, where the acid-induced self-assembly of POM resulted in an enhanced absorption peak (Figure 1h). The significant blue-shift towards 808 nm, one of the most widely clinically used NIR lasers, makes these clusters a promising photothermal agent for tumor ablation therapy.

Ox-POM clusters were incubated with varying concentrations of GSH (control, 2, 10, and 15 mM) to evaluate their redox-activated PA imaging performance. Representative PA images of the four samples with 870 nm excitation are shown in Figure 2a. No PA signal was detected for pure *Ox*-POM without GSH incubation. The samples with higher levels of reduction exhibited higher PA signal intensities, further confirmed by the PA spectra of the sample solutions (Figure 2b). Furthermore, the photothermal conversion performance of these samples was investigated under 808 nm laser irradiation at a power density of 1.5 W/cm^2. As shown in Figure 2c–d, the co-culture solutions with higher GSH concentrations showed higher temperatures of up to 55 °C within 5 min of irradiation, while the temperature of *Ox*-POM without GSH showed little change, demonstrating that the clusters after redox-activation can efficiently convert NIR laser energy into thermal energy. More detailed experiments revealed that the temperature enhancement was proportional to the concentration of clusters and the power density of the laser (Figure S8).

The blue-shift toward 808 nm (Figure 1h) of *Ox*-POM after redox activation motivated us to investigate the photothermal performance of these clusters at different pH values (pH = 4.0, 6.5, 7.4, and pure PBS of pH = 7.4). Such blue-shift from ~1030 nm toward 808 nm was observed because the gap between the highest occupied molecular orbital and the lowest unoccupied molecular orbital was broadened by the acidity *via* the protonation of the edge-sharing oxygen atoms.[37] A more efficient photothermal conversion under 808 nm laser irradiation was obtained at lower pH values (Figure S9), highlighting the potential of these agents as promising agents for PTT cancer treatment since the pH in the tumor

microenvironment is usually lower than that in normal tissues.[39] In addition, the recycling temperature variations of the cluster dispersion were explored to evaluate the photothermal stability of these clusters under 808 nm laser irradiation for 5 min, followed by natural cooling to room temperature for five laser on/off cycles. No deterioration of the clusters' photothermal performance was found during the recycling (Figure S10), which indicates the durable photothermal properties of these clusters.

The *in vitro* toxicity of *Ox*-POM was tested by a standard MTT assay after incubation of the clusters at varying concentrations (0, 50, 100, 250, and 500 μg/mL) with human embryonic kidney 293 (HEK293) and murine breast cancer 4T1 cells for 24 h and 48 h. The *Ox*-POM showed negligible toxicity in both cell lines, even at a high concentration of 500 μg/mL (Figure S11). Subsequently, the *Ox*-POM clusters reduced by different concentrations of GSH (5, 10, and 15 mM) were added into cell culture plates containing 4T1 cells, followed by irradiation with an 808 nm laser for 5 min. As shown in Figure 3a, with stronger reducing conditions or higher concentrations of *Ox*-POM clusters, more cells were killed upon NIR laser irradiation at the power density of 1.5 W/cm^2. Furthermore, 4T1 cells were then treated with 808 nm laser of various power densities (0.7, 1.0, and 2.0 W/cm^2) and a constant level of *Ox*-POM. It was found that the relative viabilities of the 4T1 cells decreased remarkably at elevated power density, as well as at higher cluster concentration levels (Figure 3b). In contrast, negligible cell killing was found for the groups without any treatment or treatment with NIR laser only. The cancer cells were also stained with trypan blue to differentiate dead cells from live cells (Figure 3c), corroborating the MTT results. These findings clearly demonstrate that the *Ox*-POM clusters reduced by GSH can be used as an effective photothermal agent for cancer cell ablation.

With encouraging *in vitro* findings, the circulation, biodistribution, and clearance of *Ox*-POM clusters were investigated via positron emission tomography (PET) imaging, a powerful, quantitative, and non-invasive imaging technique. The oxygen-rich *Ox*-POM clusters can be conveniently labeled with the highly oxophilic radionuclide ^{89}Zr (in the chemical form of $^{89}Zr^{4+}$),[40, 41] and the labeling yield herein was measured to be as high as 90.4% (Figure S12). After intravenous injection of ~ 5 MBq of ^{89}Zr-*Ox*-POM clusters into BALB/c mice, PET imaging was performed at various time points. Interestingly, the ultra-small sized ^{89}Zr-*Ox*-POM showed low accumulation in the liver and spleen and was mainly excreted by the kidneys as strong PET signal was found in both the kidneys and bladder (Figure 4a). Our results consistent with previous reports that ultra-small sized particles (hydrodynamic size <5.5 nm) can escape from recognition and capture by the liver and are cleared via the kidneys, which filters metabolites from the bloodstream through the approximately 10 nm pores of the basal lamina.[42] Quantitative data obtained from region-of-interest (ROI) analysis of these PET images indicated the excellent *in vivo* circulation behavior of these clusters with a long half-life of 2.79 ± 0.47 h (Figure 4b), which is highly desirable for both active and passive targeting of tumor tissue. The time point of the highest kidney uptake was 6 h postinjection (p.i.), at 23.7 ± 3.1 % ID/g, while the signals in the liver and spleen decreased gradually over the first 24 hours (Figure 4c). To further confirm the accuracy of PET quantification analysis, *ex vivo* biodistribution studies were carried out at 24 p.i. As shown in Figure 4d, the kidney uptake at 24 h p.i. of ^{89}Zr-*Ox*-POM was 17.5 ± 3.2 % ID/g, while the accumulation in the liver and spleen was relatively low, with values

of 8.7 ± 0.7 and 3.1 ± 1.1 % ID/g, respectively (n = 3). These results show that the clusters have excellent *in vivo* pharmacokinetic properties and can overcome the limitations of high uptake by mononuclear phagocyte systems (e.g., liver/spleen) and long *in vivo* retention time of many commonly-used nanoparticles.

The efficient redox-activated self-assembly of *Ox*-POM, strong photothermal conversion, and excellent *in vivo* pharmacokinetics encouraged us to employ *Ox*-POM for *in vivo* PA imaging-guided photothermal therapy of cancer. *In vivo* redox-activated PA imaging was conducted on 4T1-tumor-bearing mice prior to, and at 1 h, 3 h, 6 h, and 24 h after intravenous injection of *Ox*-POM clusters. As shown in Figure 5a, the PA signal was detected in the tumors as early as 1 h p.i., demonstrating the strong redox-activated effect of *Ox*-POM by the tumor redox status, which is regarded as one of the several physiologic properties differing tumor and normal tissues.[43, 44] The signal intensity increased gradually from 1 h to 6 h p.i. (Figure S13) and showed excellent tumor tissue penetration. As both the extracellular tumor milieu (pH = 6.5 – 6.8) and endocytic organelles (pH = 5.0 – 6.0) in the tumor endothelial cells show a pH drop,[1,39,45] the POM clusters can self-assemble into nano-aggregates in the tumor tissue to enhance tumor retention over time, which has been confirmed by TEM imaging of tumor tissues,[37] as well as strong PA signal at an extended time of 24 h p.i. (Figure 5a). In line with the aforementioned *in vitro* results, these *in vivo* results confirm the pH-responsive self-assembly and redox-activated effect of *Ox*-POM clusters in the acidic and reducing tumor microenvironment.

Taking advantage of such redox-activated effects, *in vivo* photothermal imaging and therapy were performed under the exposure of an 808 nm laser for 5 min at 6 h p.i. of *Ox*-POM, as this time point demonstrated peak uptake of the nanoclusters in the tumor. The tumor temperature and thermal images were visualized with a thermal camera. As shown in Figure 5b, the temperature of the tumor rapidly increased to above 40 °C in 30 s and reached 52 °C in 5 min under laser irradiation, which is sufficient to thermally ablate the tumor, while the control group showed only limited temperature increase (Figure S14). For the treated group, 4T1 tumor growth was completely eliminated without subsequent recurrence for a prolonged period of up to 2 months (Figure 5c–e, Figures S15–16), whereas the control groups demonstrated rapid tumor growth. Hematoxylin and eosin (H&E) staining of tumors from different groups further confirmed the above results, where the treatment group shows the most tumor damage (Figure 5f). No abnormal behavior or significant weight loss was observed in any group (Figure S17), indicating minimal side effects of the clusters. The H&E stained images of different organs (heart, liver, spleen, lung, and kidney) showed no noticeable organ damage or inflammatory lesions over 30 days (Figure S18), suggesting the low *in vivo* toxicity of these clusters to normal tissue.

CONCLUSION

In summary, we present here the redox-activated *Ox*-POM clusters for tumor microenvironment-responsive PA imaging-guided tumor ablation, which exhibits high-performance PA imaging with outstanding photothermal conversion efficiency. The ultra-small *Ox*-POM clusters can escape from recognition and capture by the liver and spleen and are mainly excreted through the kidneys, which is highly desirable for reducing the potential

toxic effects caused by the long-term accumulation of nanoparticles in various organs. Importantly, with long *in vivo* circulation half-life, these bioresponsive clusters can be passively accumulated in the tumor due to the EPR effect, self-assemble into larger nano sizes under the tumor's acidic environment, and be reduced to NIR absorptive agents for efficient PA imaging-guided PTT of cancer, as was demonstrated by various *in vitro* and *in vivo* experiments. As a proof-of-concept, this finding is expected to establish a new class of redox-activated probes based on clusters, bridging the conventional concepts of "molecule" and "nano" in the bio-imaging field.

Supplementary Material

Refer to Web version on PubMed Central for supplementary material.

Acknowledgments

This work was supported, in part, by the University of Wisconsin - Madison, the National Institutes of Health (NIBIB/NCI 1R01CA169365, 1R01EB021336, P30CA014520, S10-OD018505, T32GM008505), and the American Cancer Society (125246-RSG-13-099-01-CCE).

References

1. Mi P, Kokuryo D, Cabral H, Wu H, Terada Y, Saga T, Aoki I, Nishiyama N, Kataoka K. Nat Nanotechnol. 2016; 11:724–730. [PubMed: 27183055]
2. Chen Y, Ye D, Wu M, Chen H, Zhang L, Shi J, Wang L. Adv Mater. 2014; 26:7019–7026. [PubMed: 25156250]
3. Yavuz MS, Cheng Y, Chen J, Cobley CM, Zhang Q, Rycenga M, Xie J, Kim C, Song KH, Schwartz AG, Wang LV, Xia Y. Nat Mater. 2009; 8:935–939. [PubMed: 19881498]
4. Lu Y, Aimetti AA, Langer R, Gu Z. Nat Rev Mater. 2016; 2:16075.
5. Sarsour EH, Kumar MG, Chaudhuri L, Kalen AL, Goswami PC. Antioxid Redox Signal. 2009; 11:2985–3011. [PubMed: 19505186]
6. Rubartelli A, Lotze MT. Trends Immunol. 2007; 28:429–436. [PubMed: 17845865]
7. Lee MH, Yang Z, Lim CW, Lee YH, Dongbang S, Kang C, Kim JS. Chem Rev. 2013; 113:5071–5109. [PubMed: 23577659]
8. Zhao Z, Fan H, Zhou G, Bai H, Liang H, Wang R, Zhang X, Tan W. J Am Chem Soc. 2014; 136:11220–11223. [PubMed: 25061849]
9. Lim SY, Hong KH, Kim DI, Kwon H, Kim HJ. J Am Chem Soc. 2014; 136:7018–7025. [PubMed: 24754635]
10. Tang Y, Song H, Su Y, Lv Y. Anal Chem. 2013; 85:11876–11884. [PubMed: 24236771]
11. Loving GS, Mukherjee S, Caravan P. J Am Chem Soc. 2013; 135:4620–4623. [PubMed: 23510406]
12. Deng R, Xie X, Vendrell M, Chang YT, Liu X. J Am Chem Soc. 2011; 133:20168–20171. [PubMed: 22107163]
13. Nie L, Chen X. Chem Soc Rev. 2014; 43:7132–7170. [PubMed: 24967718]
14. Wang LV, Hu S. Science. 2012; 335:1458–1462. [PubMed: 22442475]
15. Kim JW, Galanzha EI, Shashkov EV, Moon HM, Zharov VP. Nat Nanotechnol. 2009; 4(10):688–694. [PubMed: 19809462]
16. Sun C, Wen L, Zeng J, Wang Y, Sun Q, Deng L, Zhao C, Li Z. Biomaterials. 2016; 91:81–89. [PubMed: 27017578]
17. De la Zerda A, Zavaleta C, Keren S, Vaithilingam S, Bodapati S, Liu Z, Levi J, Smith BR, Ma TJ, Oralkan O, Cheng Z, Chen X, Dai H, Khuri-Yakub BT, Gambhir SS. Nat Nanotechnol. 2008; 3:557–562. [PubMed: 18772918]

18. Xie L, Wang G, Zhou H, Zhang F, Guo Z, Liu C, Zhang X, Zhu L. Biomaterials. 2016; 103:219–228. [PubMed: 27392290]
19. De la Zerda A, Liu Z, Bodapati S, Teed R, Vaithilingam S, Khuri-Yakub BT, Chen X, Dai H, Gambhir SS. Nano Lett. 2010; 10:2168–2172. [PubMed: 20499887]
20. Chen YS, Frey W, Kim S, Kruizinga P, Homan K, Emelianov S. Nano Lett. 2011; 11:348–354. [PubMed: 21244082]
21. Liu Y, He J, Yang K, Yi C, Nie L, Khashab NM, Chen X, Nie Z. Angew Chem Int Ed. 2015; 54:15809–15812.
22. Du Y, Jiang Q, Beziere N, Song L, Zhang Q, Peng D, Chi C, Yang X, Guo H, Diot G, Ntziachristos V, Ding B, Tian J. Adv Mater. 2016; 28:10000–10007. [PubMed: 27679425]
23. Zhang L, Su H, Cai J, Cheng D, Ma Y, Zhang J, Zhou C, Liu S, Shi H, Zhang Y, Zhang C. ACS Nano. 2016; 10:10404–10417. [PubMed: 27934087]
24. Zha Z, Zhang S, Deng Z, Li Y, Li C, Dai Z. Chem Commun. 2013; 49:3455–3457.
25. Chen J, Liu C, Hu D, Wang F, Wu H, Gong X, Liu X, Song L, Sheng Z, Zheng H. Adv Funct Mater. 2016; 26:8715–8725.
26. Lv G, Guo W, Zhang W, Zhang T, Li S, Chen S, Eltahan AS, Wang D, Wang Y, Zhang J, Wang PC, Chang J, Liang XJ. ACS Nano. 2016; 10:9637–9645.
27. Lovell JF, Jin CS, Huynh E, Jin H, Kim C, Rubinstein JL, Chan WC, Cao W, Wang LV, Zheng G. Nat Mater. 2011; 10:324–332. [PubMed: 21423187]
28. Pu K, Shuhendler AJ, Jokerst JV, Mei J, Gambhir SS, Bao Z, Rao J. Nat Nanotechnol. 2014; 9:233–239. [PubMed: 24463363]
29. Miao Q, Lyu Y, Ding D, Pu K. Adv Mater. 2016; 28:3662–3668. [PubMed: 27000431]
30. Li LL, Ma HL, Qi GB, Zhang D, Yu F, Hu Z, Wang H. Adv Mater. 2016; 28:254–262. [PubMed: 26568542]
31. Wang L, Yang PP, Zhao XX, Wang H. Nanoscale. 2016; 8:2488–2509. [PubMed: 26757620]
32. Dragulescu-Andrasi A, Kothapalli SR, Tikhomirov GA, Rao J, Gambhir SS. J Am Chem Soc. 2013; 135:11015–11022. [PubMed: 23859847]
33. Zhang D, Qi GB, Zhao YX, Qiao SL, Yang C, Wang H. Adv Mater. 2015; 27:6125–6130. [PubMed: 26350172]
34. Duan Z, Gao Y-J, Qiao Z-Y, Fan G, Liu Y, Zhang D, Wang H. J Mater Chem B. 2014; 2:6271–6282.
35. Liu T, Diemann E, Li H, Dress AW, Muller A. Nature. 2003; 426:59–62. [PubMed: 14603315]
36. Liu T, Langston ML, Li D, Pigga JM, Pichon C, Todea AM, Muller A. Science. 2011; 331:1590–1592. [PubMed: 21436449]
37. Zhang C, Bu W, Ni D, Zuo C, Cheng C, Li Q, Zhang L, Wang Z, Shi J. J Am Chem Soc. 2016; 138:8156–8164. [PubMed: 27264421]
38. Buckley RI, Clark RJ. Coord Chem Rev. 1985; 65:167–218.
39. Wang Y, Zhou K, Huang G, Hensley C, Huang X, Ma X, Zhao T, Sumer BD, DeBerardinis RJ, Gao J. Nat Mater. 2014; 13:204–212. [PubMed: 24317187]
40. Shaffer TM, Wall MA, Harmsen S, Longo VA, Drain CM, Kircher MF, Grimm J. Nano Letters. 2015; 15:864–868. [PubMed: 25559467]
41. Chen F, Goel S, Valdovinos HF, Luo H, Hernandez R, Barnhart TE, Cai W. ACS Nano. 2015; 9:7950–7959. [PubMed: 26213260]
42. Choi HS, Liu W, Misra P, Tanaka E, Zimmer JP, Itty Ipe B, Bawendi MG, Frangioni JV. Nat Biotechnol. 2007; 25:1165–1170. [PubMed: 17891134]
43. Matsumoto K, Hyodo F, Matsumoto A, Koretsky AP, Sowers AL, Mitchell JB, Krishna MC. Clin Cancer Res. 2006; 12:2455–2462. [PubMed: 16638852]
44. Hyodo F, Matsumoto K, Matsumoto A, Mitchell JB, Krishna MC. Cancer Res. 2006; 66:9921–9928. [PubMed: 17047054]
45. Tannock IF, Rotin D. Cancer Res. 1989; 49:4373–4384. [PubMed: 2545340]

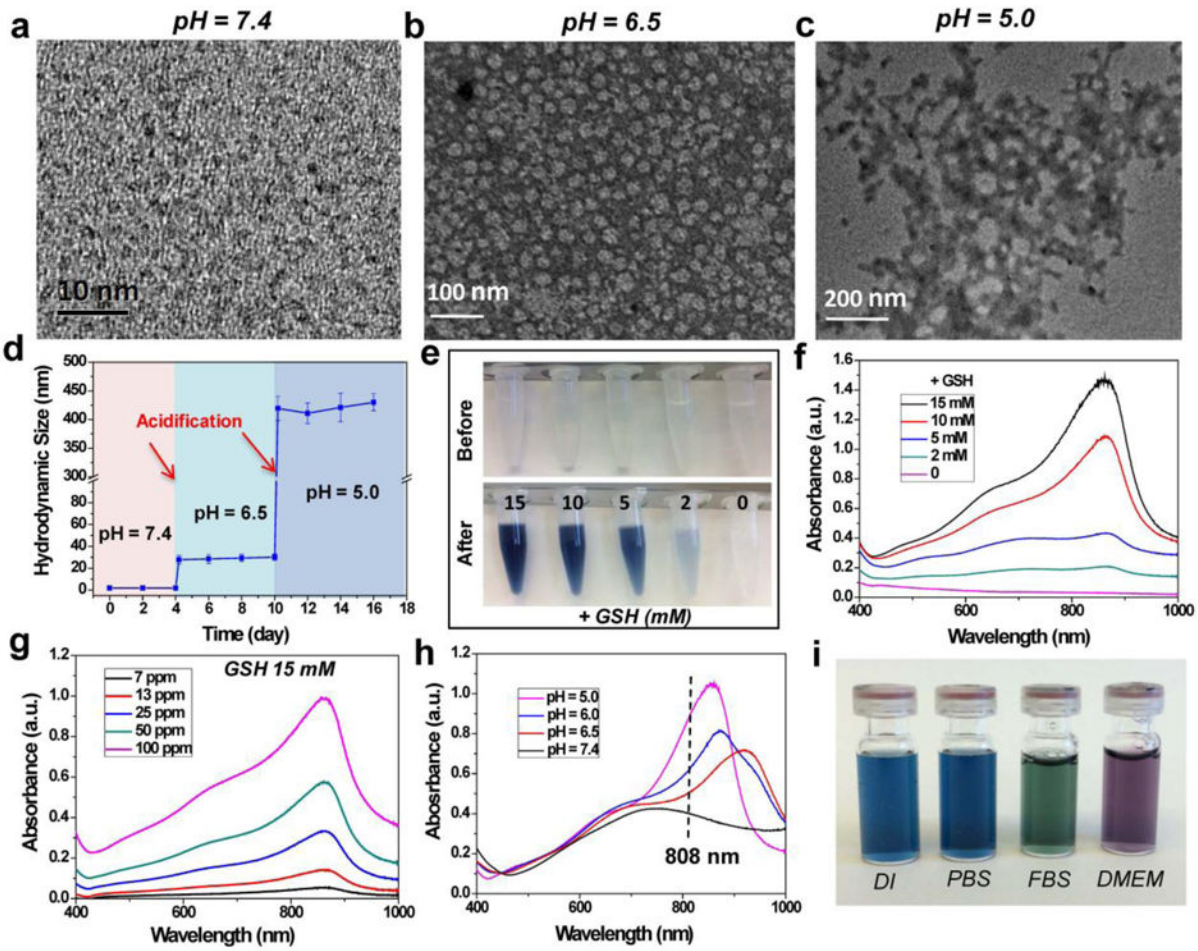

Figure 1.

Synthesis and characterization of *Ox*-POM. a - c) TEM images of clusters at pH = 7.4, 6.5, and 5.0. d) DLS measurements of *Ox*-POM clusters with successive acidifications from pH = 7.4 to pH = 6.5 and to pH = 5.0. e) Photographs of *Ox*-POM clusters dispersed in deionized water before and after incubation with various concentrations of GSH and f) the corresponding UV-vis spectra. g) UV-vis absorptions of *Ox*-POM clusters with various Mo concentrations after incubation with GSH (15 mM). h) UV−vis-NIR absorptions of *Ox*-POM clusters (100 ppm Mo) at various pH values after incubation with GSH (15 mM). i) Photographs of GSH-reduced *Ox*-POM clusters dispersed in various media.

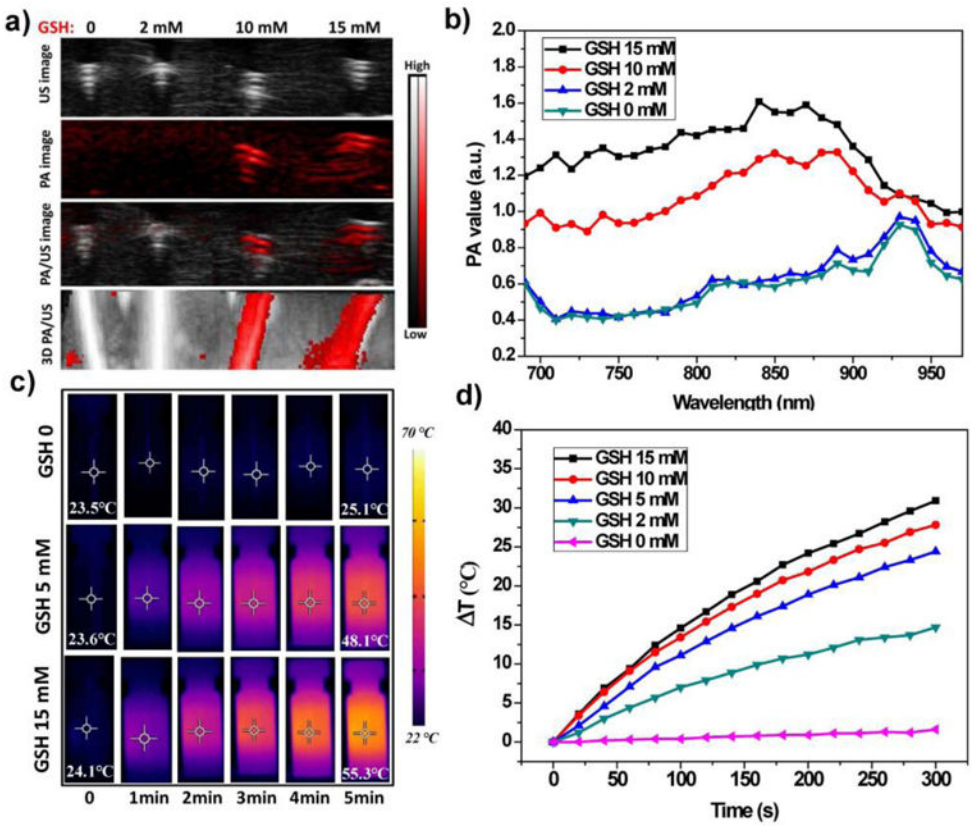

Figure 2.

Redox-activated PA and photothermal properties of *Ox*-POM clusters. a) PA imaging and b) PA spectra of *Ox*-POM clusters after incubation with various concentrations of GSH (control, 2, 10, and 15 mM). c) Thermal images of various solutions and d) photothermal heating curves of *Ox*-POM clusters (100 ppm Mo, incubated with various concentrations of GSH) with 808 nm laser irradiation for 5 min at the power intensity of 1.5 w/cm^2.

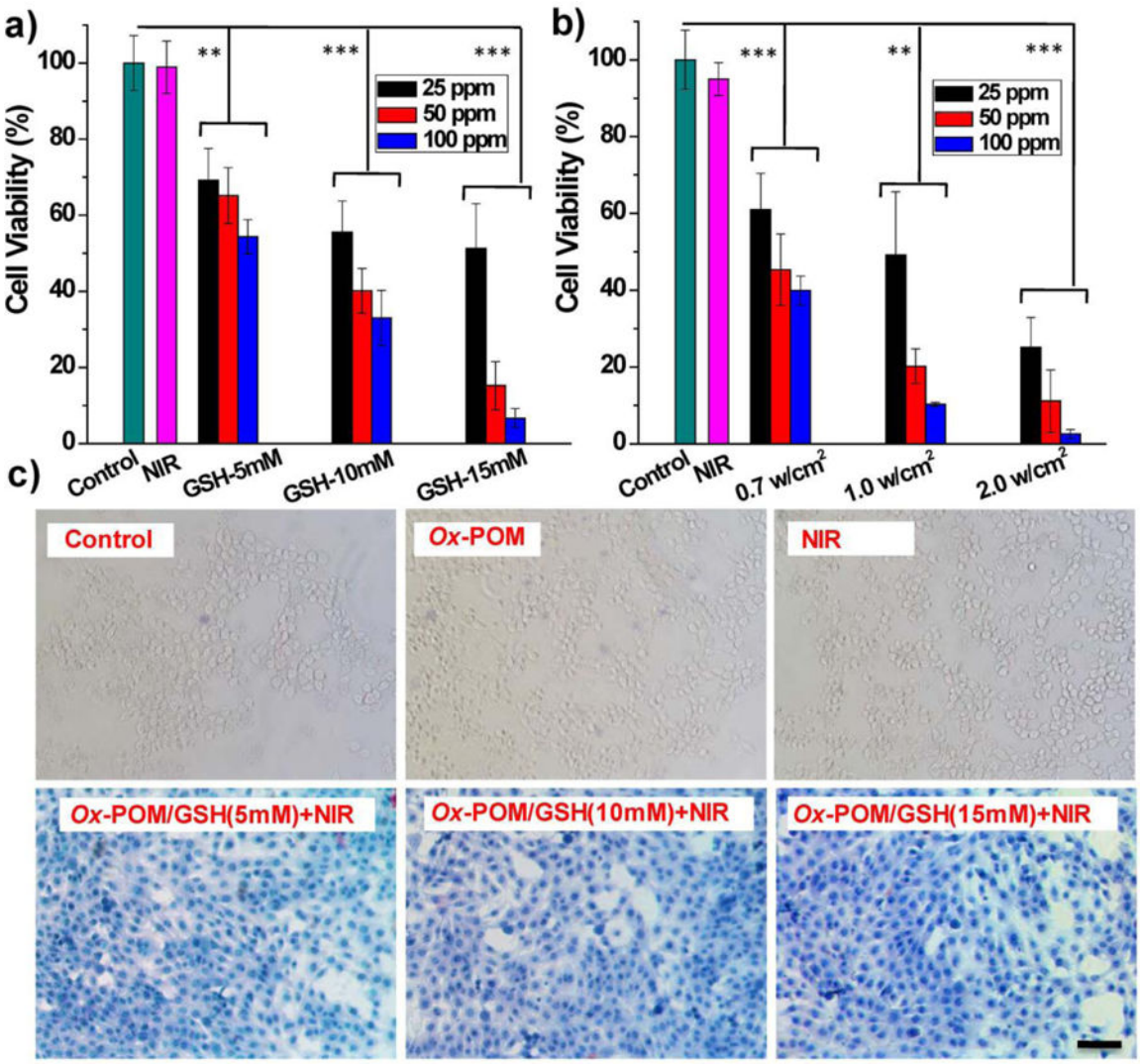

Figure 3.

In vitro photothermal therapy. a) Relative viabilities of 4T1 cells after photothermal therapy at varied concentrations of *Ox*-POM in different reducing conditions (GSH: 15, 10, and 5 mM) under 808 nm NIR laser irradiation (1.5 W/cm^2) for 5 min (n = 4, mean ± s.d., *P<0.05, ***P<0.001). b) Relative viabilities of 4T1 cells after photothermal therapy at varied concentrations of *Ox*-POM reduced with 15 mM GSH under 808 nm NIR laser irradiation of various power densities (2.0, 1.0, and 0.7 W/cm^2) for 5 min (n = 4, mean ± s.d., *P<0.05, ***P<0.001). c) Optical microscopy images of trypan blue-stained cells after incubation with clusters and exposure to the 808 nm laser (1.5 W/cm^2, 5 min) at different treatment conditions. Scale bar: 100 μm.

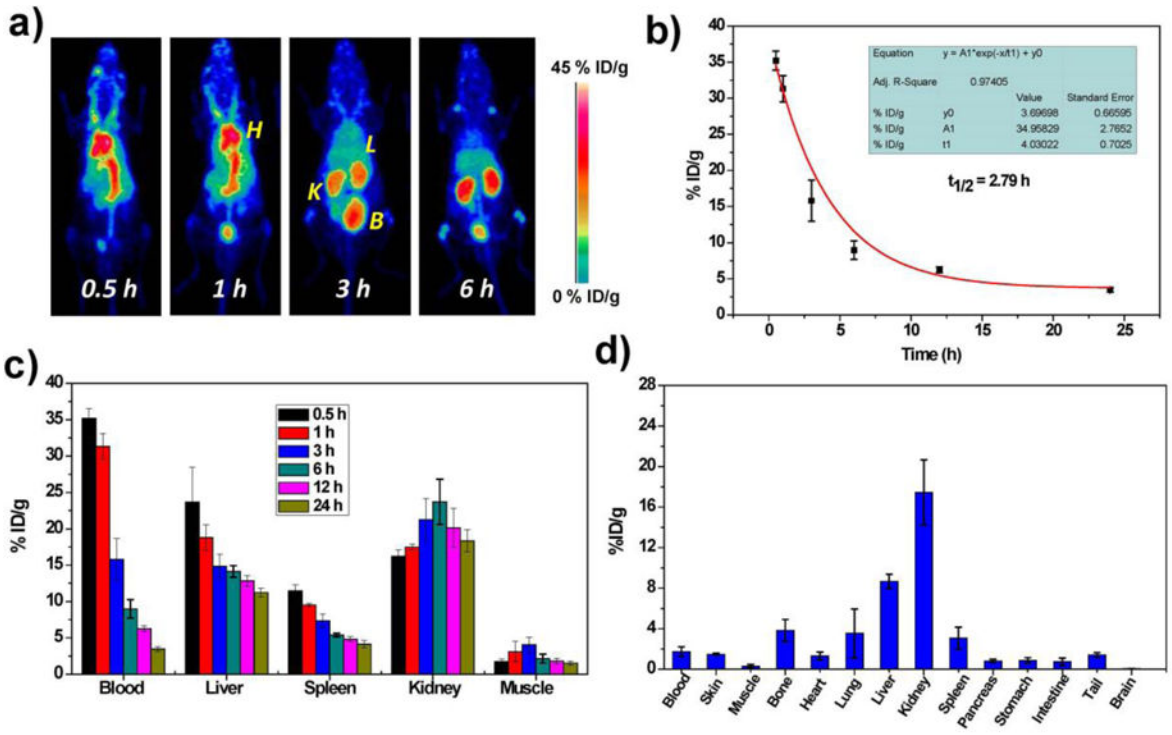

Figure 4.

In vivo studies of *Ox*-POM clusters. a) Representative maximum intensity projection PET images of mice taken at various time point post intravenous injection of ^{89}Zr-*Ox*-POM. H: heart; K: kidney; L: liver; B: bladder. b) Time-activity curves of ^{89}Zr-*Ox*-POM in the blood (n = 3, mean ± s.d.). c) Quantification of ^{89}Zr-*Ox*-POM uptake in the blood, liver, spleen, kidney, and muscle at various time points post-injection (n = 3, mean ± s.d.). d) Biodistribution of ^{89}Zr-*Ox*-POM clusters at 24 h after intravenous injection into mice as determined by ^{89}Zr radioactivity measurement in various tissues and organs (n = 3, mean ± s.d.).

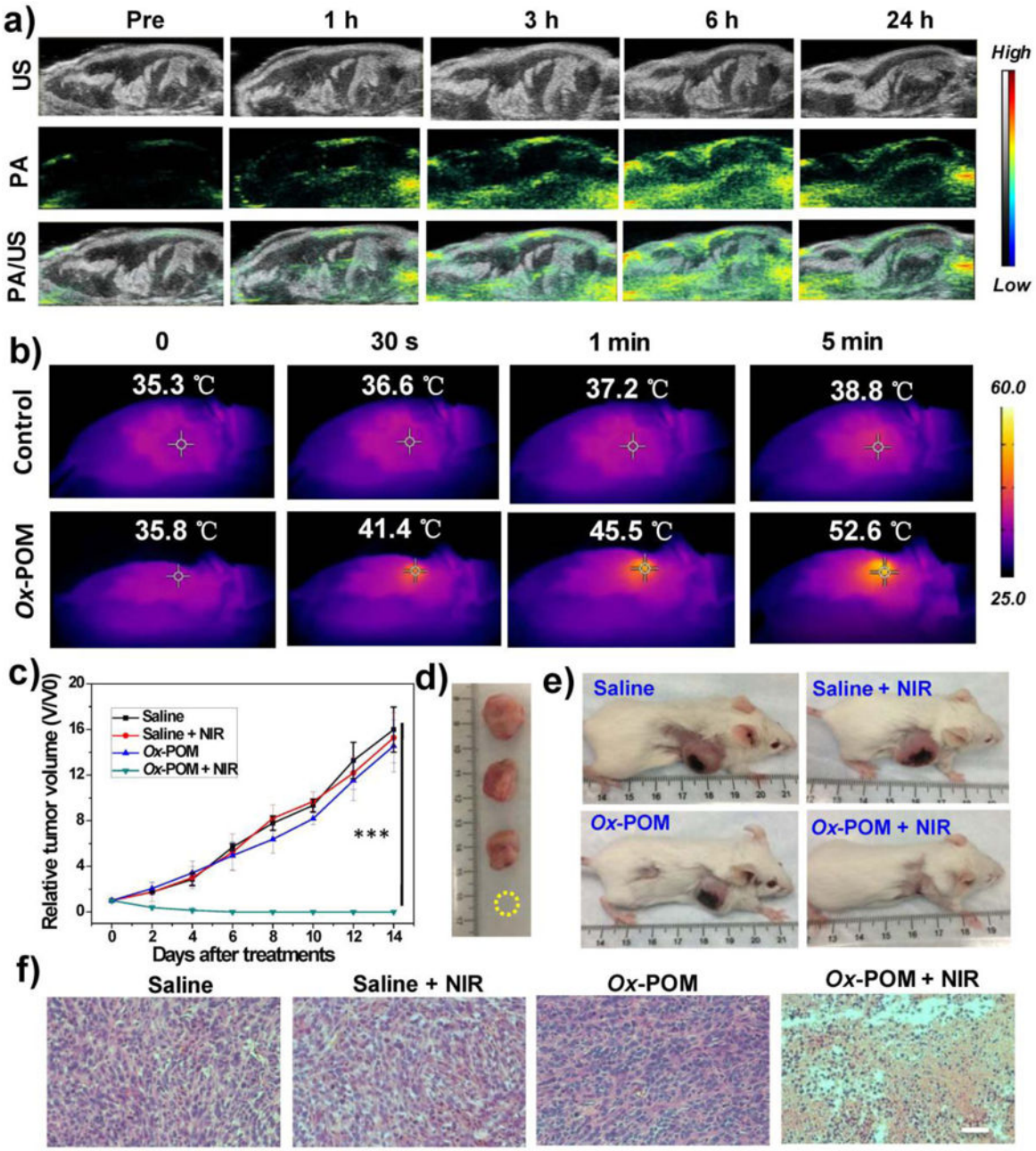

Figure 5.

In vivo PA imaging and photothermal therapy in 4T1-tumor-bearing mice. (a) *In vivo* PA images of 4T1 tumor-bearing mice before and after intravenous injection of *Ox*-POM clusters. The entire view was tumor tissues. b) Photothermal images of 4T1 tumor-bearing mice before and after intravenous injection of *Ox*-POM clusters under continuous 808 nm laser irradiation for different durations. c) Tumor growth profiles of 4T1 tumors after each treatment (n = 4, mean ± s.d., ***P<0.001). d) Representative photographs of dissected tumors and e) mice at 14 day post treatments. f) H&E staining of tumor sections after various treatments. Scale bar: 100 μm.

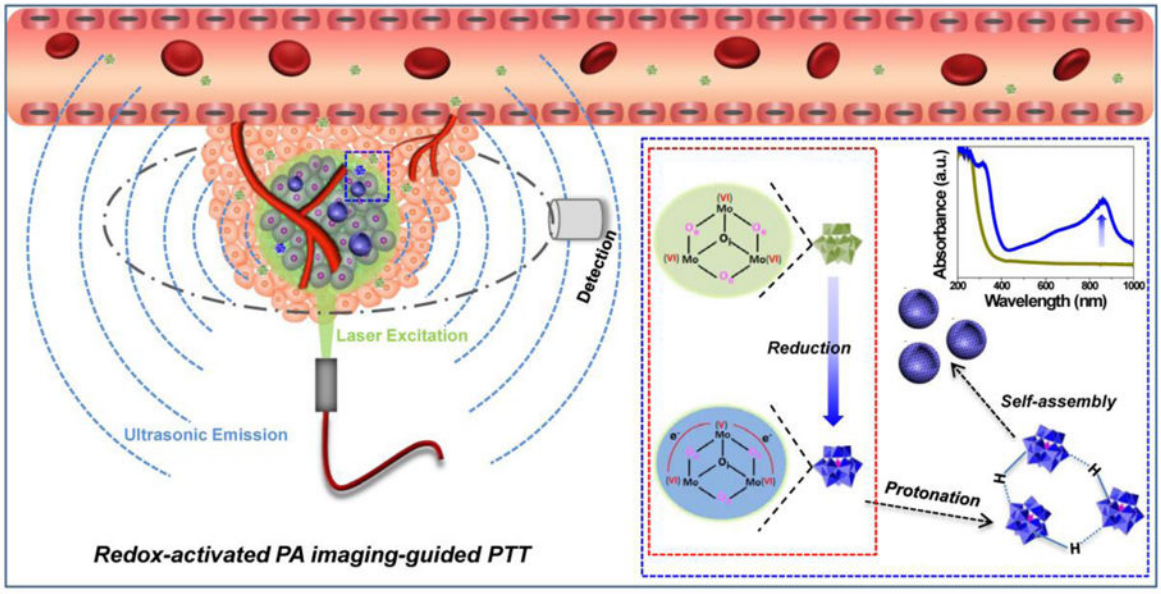

Scheme 1.

Schematic diagram of the *Ox*-POM in response to the tumor microenvironment for redox-activated PA imaging-guided PTT.